The N-terminal Region of α-Synuclein Controls Amyloid Nucleation at the Condensate Interface

Rebecca J. Thrush,[1,2] Devkee M. Vadukul,[1] Siân C. Allerton,[1,2] Marko Storch,[3,4] and Francesco A. Aprile.[1,2]*

[1]Department of Chemistry, Molecular Sciences Research Hub, Imperial College London, London W12 0BZ, UK
[2]Institute of Chemical Biology, Molecular Sciences Research Hub, Imperial College London, London W12 0BZ, UK
[3]London Biofoundry, Translation and Innovation Hub, Imperial College London, London W12 0BZ, UK
[4]Department of Infectious Disease, South Kensington, Imperial College London, London SW7 2AZ, UK

ABSTRACT

α-Synuclein can self-assemble into amyloid fibrils in neurodegenerative diseases, including Parkinson's disease. Recent studies show α-synuclein can undergo liquid-liquid phase separation, forming biomolecular condensates. The interconnection between α-synuclein amyloid formation and liquid-liquid phase separation is evident as these condensates can mature into solid gel-like condensates containing amyloid fibrils. Among the many α-synuclein post-translational modifications, N-terminally truncated fragments have been found in aggregates isolated from Parkinson's disease affected brains and are known to affect the *in vitro* aggregation kinetics.

Here, we show that physiologically relevant N-terminal truncation of residues 1-4 significantly enhances α-synuclein aggregation. Combining amyloid aggregation and liquid-liquid phase separation studies, we determined that this truncation increases the propensity of α-synuclein to nucleate at the interface, specifically at the fibril surface, on lipid vesicles and at the interface of biomolecular condensates. Our results enhance the understanding of α-synuclein pathology and offer new targets for therapeutic treatment.

INTRODUCTION

The intrinsically disordered protein (IDP) α-synuclein (α-syn) exists as a monomer and multimers in neurons, where it mediates neurotransmitter release and synaptic function[1-8]. α-Syn is also found as insoluble amyloid fibrils with a characteristic cross β-sheet rich core structure[9-12]. Aberrant accumulation of α-syn amyloid fibrils is the major hallmark of neurodegenerative diseases including Parkinson's disease (PD), dementia with Lewy bodies, and multiple system atrophy[13,14].

Many post-translational modifications (PTMs) affect α-syn amyloid aggregation and PD pathology[15-29]. These PTMs include acetylation, phosphorylation, and terminal domain truncation[17-20]. One PTM that remains largely unexplored is N-terminal truncation, which has been observed both *in vitro*[30,31] and *in vivo*[18-20,32-35]. The N-terminus of α-syn plays key roles in both the physiological and pathological functions of the protein, *e.g.*, the domain acts as a membrane anchor region[36-38], modulating synaptic vesicle fusion to the presynaptic terminal[5,39]. Yet, *in vitro* evidence shows that vesicle bound α-syn is often predisposed to self-association, and can nucleate free monomer to further promote aggregation[36,40]. The N-terminus also plays a role in the growth phase of amyloid aggregation, specifically elongation and secondary nucleation[41,42]. Thus, unsurprisingly, N-terminal truncation has been shown to alter α-syn aggregation kinetics, and amyloid morphology and stability, relative to the full-length (FL) protein[43,44]. Furthermore, deletion of resides 2–11 leads to a decrease in membrane binding affinity and toxicity in yeast[45,46]. This emphasizes the potential of N-terminal truncation to dramatically alter α-syn pathology and highlights the need to thoroughly explore the consequences of removing specific N-terminal residues.

Emerging evidence demonstrates that α-syn can undergo liquid-liquid phase separation (LLPS) *in vitro* and *in vivo*, resulting in the formation of biomolecular condensates[47-53]. α-Syn can diffuse freely within these condensates and exchange readily with the environment. Condensates can also grow *via* fusion events and Ostwald ripening[47,54]. These liquid-like properties are likely facilitated by weak, long-range interactions between α-syn molecules. With time, condensates can mature into a solid-like gel, where composing α-syn molecules exhibit reduced mobility[47,54]. This liquid-to-solid transition ultimately leads to the formation of amyloids[47,54]. Several environmental conditions can promote α-syn LLPS. A molecular crowding agent, commonly poly-ethylene glycol (PEG), is often necessary, although evaporation, a poly-cation, metal ions or other amyloidogenic proteins, *e.g.*, tau, can also induce LLPS[47,48,52-54]. The exact protein regions and interactions regulating α-syn LLPS remain largely unknown. However, the critical protein concentration required for LLPS is significantly reduced by lowering pH, increasing salt, or introducing metal ions[47,48]. Similarly, interaction of the negative C-terminus of α-syn with positively charged regions of tau or poly-L-lysine (PLK) induces complex coacervation; the co-LLPS of two opposingly charged molecules[53]. Moreover, both a variant possessing only the core residues 30–110 and C-terminally truncated α-syn undergo enhanced LLPS and aggregation, relative to FL α-syn[47,52]. Together, these findings indicate that electrostatic interactions mediate α-syn condensate formation, suggesting a key role for the terminal domains. Furthermore, β-syn, which lacks the

hydrophobic eight residue stretch located in the non-amyloid-β component (NAC) domain of α-syn, does not phase separate or aggregate, indicating that this domain is critical for LLPS[47].

Amyloid aggregation is significantly affected by conditions that promote LLPS. For several proteins, including α-syn, tau and heterogeneous nuclear ribonucleoprotein A1 (hnRNPA1), amyloid aggregation is accelerated under LLPS conditions[47,55-58]. This effect is likely due to increased local protein concentration and enhanced nucleation within condensates. Furthermore, various disease factors known to promote α-syn aggregation in the absence of LLPS (*e.g.*, Cu^{2+} and Fe^{3+}) also accelerate the onset of LLPS and the subsequent liquid-to-solid transition[47]. However, conditions that promote LLPS can also inhibit amyloid aggregation, as observed for the 42-residue-long amyloid-β peptide, which can be sequestered and stabilized within condensates formed from the low complexity domains of the DEAD-box proteins[59].

Despite the importance of the N-terminus, molecular details of how specific N-terminal regions regulate the nucleation mechanisms of α-syn self-assembly remain unclear. Here, we identify sequences within the N-terminus of α-syn that modulate specific nucleation mechanisms, including the liquid-to-solid transition following LLPS.

RESULTS AND DISCUSSION

Design of the N-terminally Truncated α-Syn Variants. Several lengths of N-terminal truncation have been associated with PD. We selected three different truncations (**Supplementary Fig. 1**): 5-140, isolated from PD brains and following *in vitro* incubation[18,31], 11-140, found in Lund human mesencephalic cells[20], and 19-140, found in human appendices[19]. We recombinantly expressed and purified all three variants, alongside FL α-syn, as confirmed by ESI-MS (**Supplementary Fig. 2**). We found that, similar to FL α-syn, all truncated variants consisted primarily of random coil secondary structure by Far-UV CD spectroscopy (**Supplementary Fig. 3**).

Truncation of the N-terminal region does not affect the ability of α-syn to undergo LLPS. α-Syn can undergo LLPS when incubated with the polycation PLK and a molecular crowding agent, *e.g.*, PEG[53]. To investigate how N-terminal truncation affects α-syn LLPS, we generated phase diagrams for our α-syn variants. We incubated varying concentrations of each protein with 10 % PEG and different concentrations of PLK for 15 min, when the highest number of condensates was observed (**Fig. 1A**). Then, we imaged the samples using differential interference contrast (DIC) microscopy, designed a General Analysis 3 (GA3) recipe that estimates condensate number and area (**Supplementary Fig. 4**), and plotted the number of condensates as a function of both α-syn and PLK concentration (**Supplementary Fig. 5**). These values were combined over 3 z-stack images taken per sample. The distance between the planes (200 μm) was selected to prevent the same object being captured in more than one image. FL α-syn formed condensates at either 40 or 60 μM with 25 μM PLK, and at 60 μM with 50 μM PLK (**Supplementary Fig. 5** and **6**). To verify that condensates contained FL α-syn, we performed fluorescence microscopy on a sample of 60 μM FL α-syn, 1 % of which was rhodamine labelled, and 25 μM PLK. Fluorescence emission was specifically localized within the condensates, confirming the presence of α-syn (**Supplementary Fig. 7**).

We repeated this analysis on 5-140, 11-140 and 19-140 α-syn. We found that all truncated variants formed condensates, with a similar dependency on the ratio of protein:PLK as FL α-syn (**Supplementary Fig. 5** and **8–10**). This suggests that residues 1–18 are not required for condensate formation, consistent with previous evidence showing that residues 30–110 are sufficient for α-syn LLPS[47].

Truncation of the N-terminal region accelerates α-syn amyloid formation under LLPS conditions. We next aimed to investigate whether N-terminal truncation affects the time-evolution of α-syn condensates. We prepared solutions containing 60 μM α-syn, 10 % PEG, and 25 μM PLK, as we observed significant condensate formation under this condition for all α-syn variants (**Supplementary Fig. 5**). We then monitored condensate maturation in the bulk of the solution using DIC microscopy and quantified condensate area and number.

First, we examined FL α-syn. We found that condensates increased in size (from ~ 1 to ~ 5 μm^2 area) during the first ~ 3 h of incubation (**Fig. 1A**,**B** and **Supplementary Fig. 11A**). This increase in size was attributed to fusion events, which can be detected after ~ 20 min (**Supplementary Fig. 12**). After ~ 3 h, the condensates stopped growing (**Fig. 1A**,**B** and **Supplementary Fig. 11A**), suggesting they had transitioned into a gel-like phase[47,54].

In contrast, the number of condensates in solution decreased continuously after 15 min. By 20 h, very few condensates were visible in the bulk solution (**Fig. 1A**,**C** and **Supplementary Fig. 11B**). This behavior was attributed in part to fusion events, which would decrease the number of condensates. We also imaged the bottom of well after 1.5 and 20 h and observed a progressive increase in surface wetting (**Fig. 1D** and **Supplementary Fig. 13**), indicating that condensate sedimentation contributes to the decay in condensate number in the bulk solution. We did not observe condensates, surface wetting, or aggregates in any of the control samples (60 μM FL α-syn alone, 25 μM PLK alone or LLPS buffer alone) within 20 h (**Supplementary Fig. 14** and **15**).

To investigate the transition of FL α-syn condensates into amyloids, we performed fluorescence emission measurements in a microplate reader using the amyloid-sensitive probe Thioflavin-T (ThT). We prepared samples containing 60 μM α-syn under the same LLPS-inducing conditions discussed above. We then recorded ThT fluorescence intensity over time as a readout of amyloid formation. To mimic the microscope set-up, we took readings every 20 min, minimizing agitation, and reduced the number of flashes per well to 30 to avoid overheating. Aggregation commenced after ~ 20 h (**Fig. 1C**). In the absence of PLK, we did not observe any significant aggregation within the time frame of this experiment (**Supplementary Fig. 16A**). These data are consistent with our microscopy observations (**Fig. 1A** and **Supplementary Fig. 13–S15**) and existing literature evidence that LLPS can accelerate amyloid aggregation[47,55-58].

To characterize the aggregates formed following LLPS, we analyzed the endpoint of this assay. DIC microscopy showed the presence of large objects with protruding fibrils (**Fig. 1E** and **Supplementary Video 1**). These aggregates were ThT-positive by fluorescent microscopy (**Fig. 1E** and **Supplementary Video 1**). TEM also confirmed the presence of fibrils in the bulk solution (**Fig. 1F**). To understand the composition and secondary structure of the aggregates we isolated and analyzed the insoluble protein fraction. We found that this fraction contained α-syn and displayed β-sheet secondary structure, as assessed by dot-blot and far-UV CD spectroscopy, respectively (**Supplementary Fig. 17**). Altogether these data indicated that amyloid aggregates were formed under LLPS conditions. In the absence of PLK, we observed a small number of thin fibrils by TEM, consistent with the ThT intensity data (**Supplementary Fig. 18**).

We repeated this analysis on 5-140, 11-140 and 19-140 α-syn. 5-140 α-syn condensates showed similar trends in their growth and number decay as FL α-syn, while 11-140 α-syn, and particularly 19-140 α-syn, condensates grew and decreased in number more slowly (**Fig. 2A**,**B** and **Supplementary Fig. 19** and **20**). We imaged the samples at 20 h using DIC microscopy and TEM. DIC microscopy at the bottom of the well showed clear surface wetting for 11-140 and 19-140 α-syn and spherical objects with protruding fibrils for 5-140 α-syn (**Fig. 2B**,**C**). Both microscopy techniques indicated that all truncated variants generated a higher yield of aggregates than FL α-syn, suggesting the truncated variants undergo a faster liquid-to-solid transition. In particular 5-140 α-syn, which generated a large network of spherical objects with protruding fibrils (**Fig. 2B**,**C**). We did not observe condensates, surface wetting, or aggregates within 20 h in the absence of PLK for all truncated variants (**Supplementary Fig. 20** and **21**).

Finally, we examined amyloid formation under LLPS conditions using the ThT intensity assay. We observed enhanced aggregation kinetics for all truncated variants, relative to FL α-syn (**Fig. 3A** and **Supplementary Fig. 16B**). DIC, ThT fluorescence and electron microscopy at the endpoint of aggregation revealed extensive, ThT-positive, thick fibril network formation for each variant (**Fig. 3B** and **Supplementary Video 2**, **3**, **4**). Again, the insoluble protein fractions were α-syn positive and contained β-sheet secondary structure, indicative of amyloids (**Supplementary Fig. 17**). Truncated α-syn incubated without PLK formed few, thin fibrils during the ThT intensity assay, consistent with their reduced aggregation kinetics relative to incubation in the presence of PLK (**Supplementary Fig. 22**).

Overall, the N-terminally truncated variants have an accelerated rate of LLPS-induced aggregation compared to FL α-syn. This may be a direct consequence of the reduced ability of their condensates to undergo growth and surface wetting, resulting in an increased lifetime of smaller, soluble condensates in the bulk solution with higher surface:volume ratios. Recent evidence suggests amyloid formation can occur at the condensate interface[47,49,58-60]. Thus, the persistence of high surface:volume ratios may accelerate the surface-dependent amyloid aggregation of the N-terminally truncated α-syn variants. Interestingly, 5-140 α-syn displayed enhanced aggregation despite its comparable condensate lifetime in solution to FL α-syn.

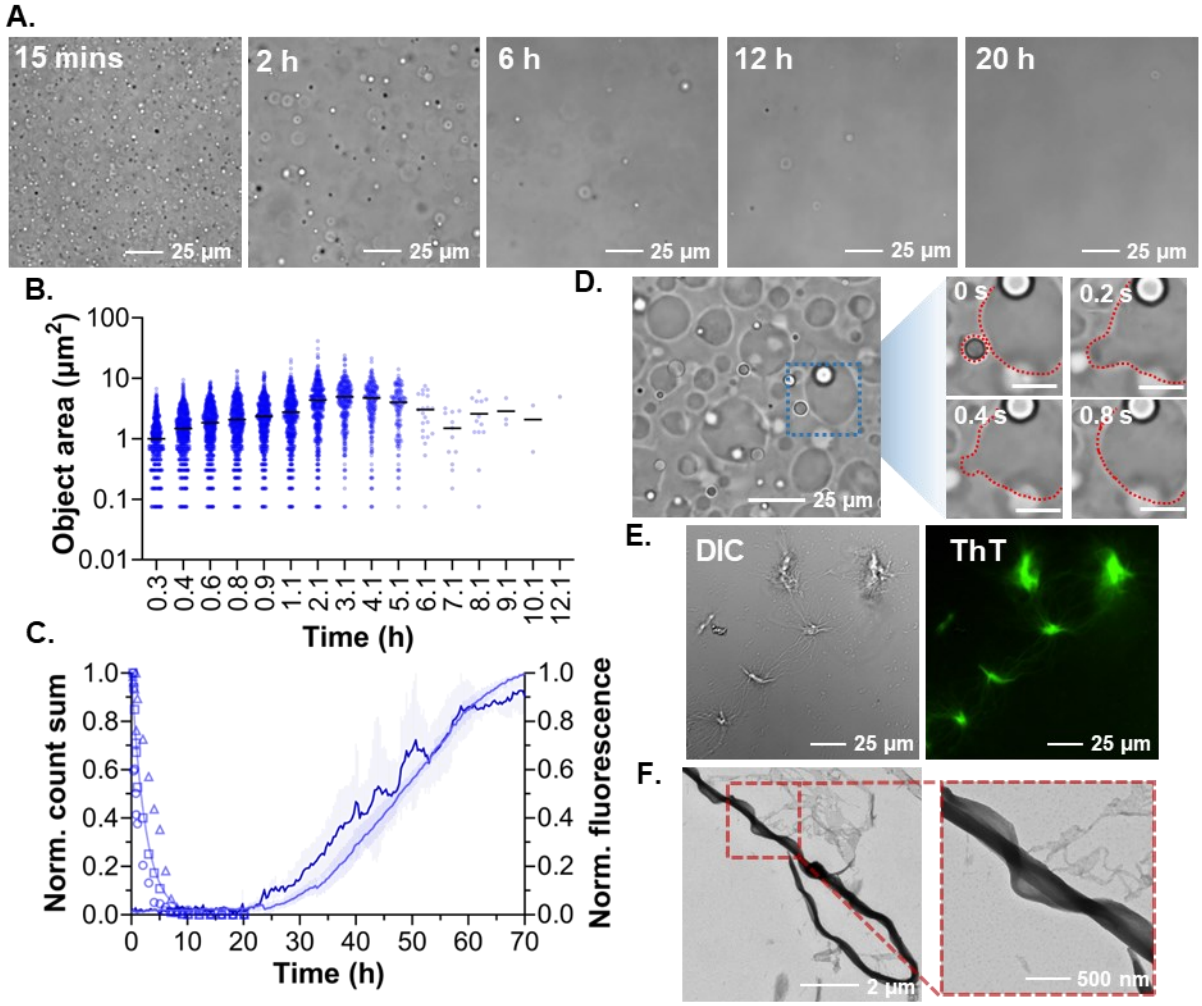

Figure 1. The incubation of FL α-syn under LLPS promoting conditions. A. Representative DIC images of 60 µM FL α-syn incubated with 25 µM PLK in LLPS buffer. Samples were incubated at 37 °C for ~ 20 h, selected time points are shown. **B.** A representative plot of the object area distribution, compiled over the 3 z-stack images acquired per time point, against time for 60 µM FL α-syn incubated with 25 µM PLK in LLPS buffer at 37 °C. The mean area at each time point is indicated by a solid black line. **C.** The normalized total object count against time, and the corresponding global fit, overlayed with LLPS aggregation data for 60 µM FL α-syn incubated at 37 °C with 25 µM PLK and 20 µM ThT in LLPS buffer. Three individual biological replicates of the normalized total object count (summed over the 3 z-stack images taken per time point) are shown, represented by circular, square or triangular symbols (see **Supplementary Fig. 13** for an expanded plot). For the LLPS aggregation data, the mean and standard deviation (represented by semi-transparent error bars) of three technical replicates, for two individual biological repeats, are shown in different shades of blue. **D.** DIC image taken at the bottom of the well after ~ 1.5 h incubation of 60 µM FL α-syn with 25 µM PLK in LLPS buffer at 37 °C. The magnified images depict a fusion event between a condensate in solution and a pre-existing area of wetting on the surface of the well (scale bars represent 10 µm). **E.** Representative DIC (left) and fluorescent (right) images of 60 µM FL α-syn with 25 µM PLK. Images are of the bottom of the well and were taken at the endpoint of a LLPS ThT aggregation assay. **F.** Representative TEM images of 60 µM FL α-syn with 25 µM PLK. An aliquot of the whole solution was collected at the endpoint of a LLPS ThT aggregation assay and imaged.

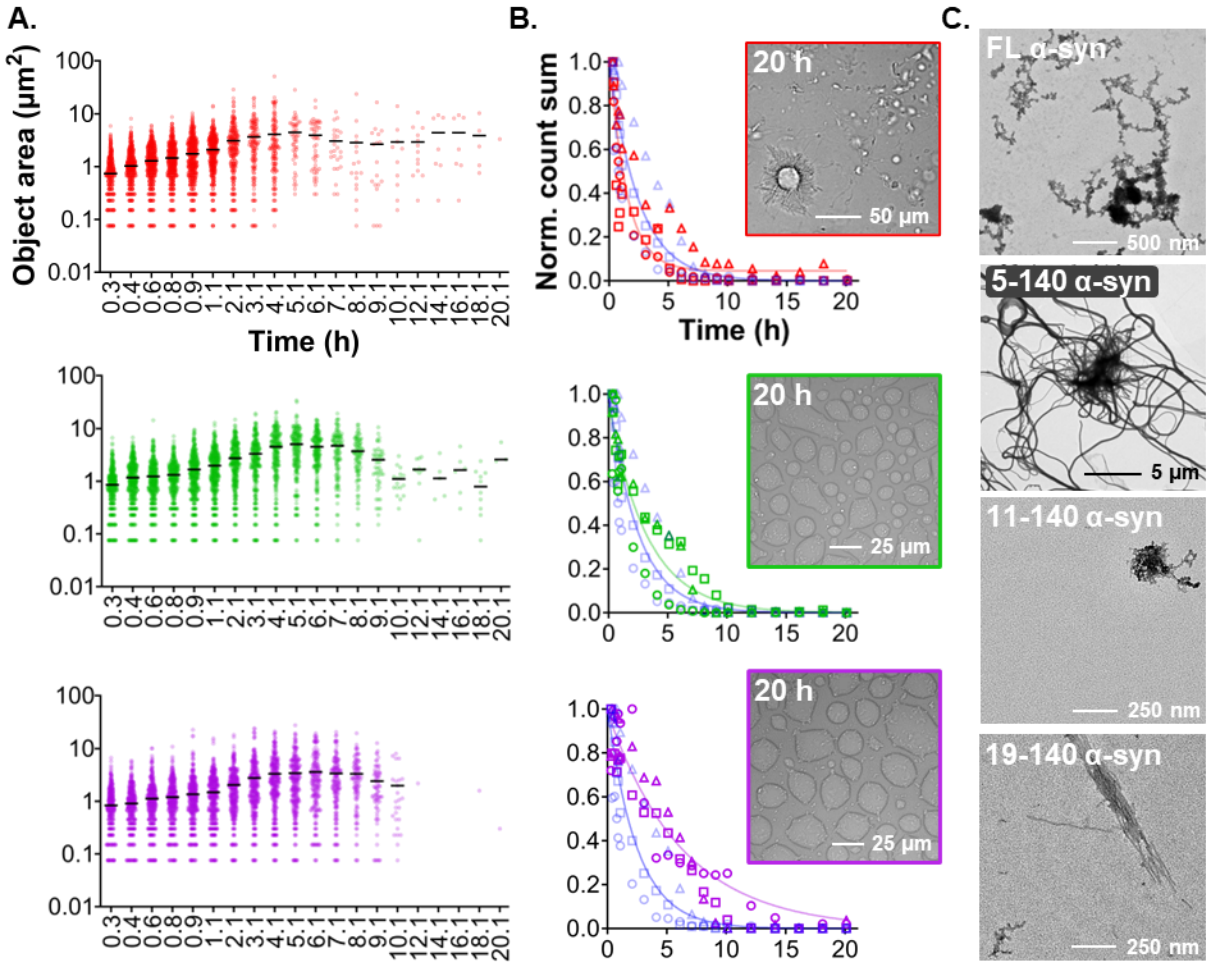

Figure 2. The incubation of truncated α-syn under LLPS promoting conditions. A. A representative plot of the object area distribution, compiled over the 3 z-stack images acquired per time point, against time for 60 μM 5-140 (red), 11-140 (green) and 19-140 (purple) α-syn incubated at 37 °C with 25 μM PLK in LLPS buffer. The mean area at each time point is indicated by a solid black line. **B.** The normalized total object count against time for 60 μM 5-140 (red), 11-140 (green) and 19-140 (purple) α-syn incubated at 37 °C with 25 μM PLK in LLPS buffer. Individual biological replicates are shown (n = 3), represented by circular, square or triangular symbols. Data are globally fit with a one-phase decay curve (solid line). The corresponding FL α-syn data (semi-transparent blue) are also shown. Overlayed are representative DIC images taken at the bottom surface of the well at the endpoint of this assay. **C.** Representative TEM images of 60 μM α-syn with 25 μM PLK in LLPS buffer. Aliquots of the whole solution were taken after 20 h incubation at 37 °C and applied to the TEM grid.

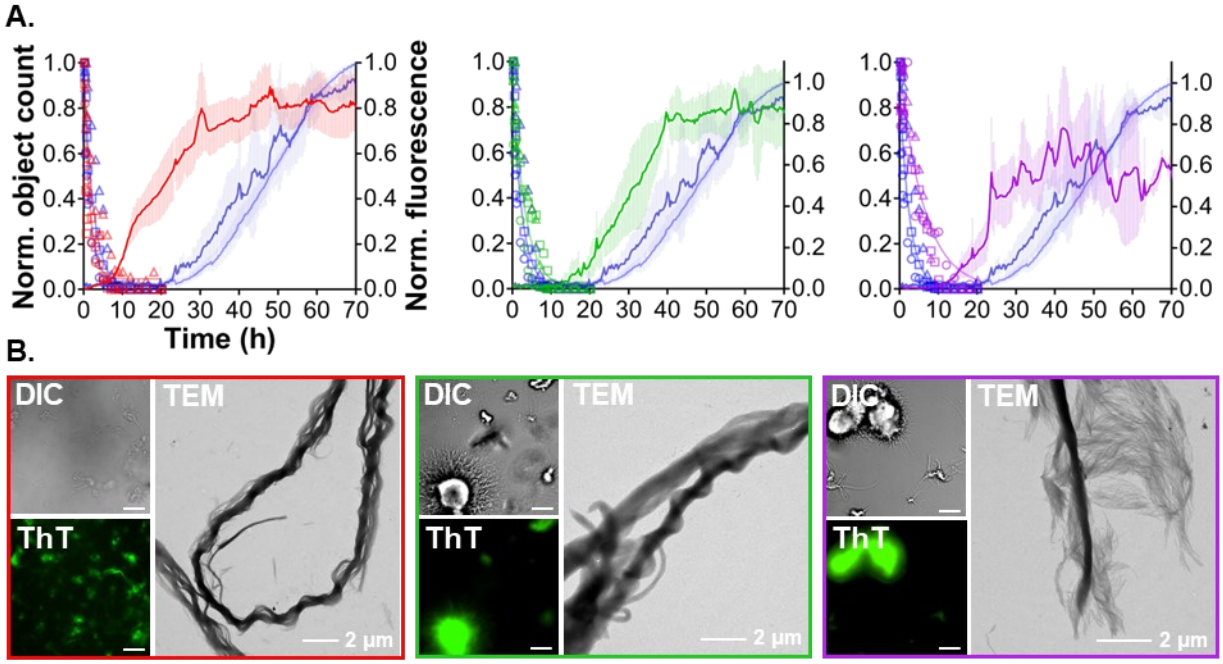

Figure 3. LLPS-induced aggregation of N-terminally truncated α-syn. A. The normalized total object count over time, and the corresponding global fit, overlayed with LLPS aggregation data for 60 µM α-syn incubated at 37 °C with 25 µM PLK and 20 µM ThT in LLPS buffer. 5-140 (red), 11-140 (green) or 19-140 (purple) α-syn are shown alongside FL α-syn (semi-transparent blue). Individual biological replicates (n = 3) of the normalized total object count (summed over the 3 z-stack images taken per time point) are represented by circular, square or triangular symbols. The LLPS aggregation data for two (FL α-syn) or one (truncated α-syn) individual biological repeats are shown, represented by their mean and standard deviation (semi-transparent error bars, n = 3). **B.** Representative DIC and ThT fluorescence images taken at the bottom of the well at the endpoint of a LLPS aggregation assay (scale bars represent 25 µm), alongside TEM images of samples of the whole solution. Samples consist of 60 µM 5-140 (red), 11-140 (green) or 19-140 (purple) α-syn incubated at 37 °C with 25 µM PLK in LLPS buffer.

The N-terminal region of α-syn regulates the nucleation and propagation of amyloid fibrils. Our final aim was to analyze the microscopic steps of amyloid aggregation, as to better understand the LLPS aggregation behavior of the truncated variants, particularly 5-140 α-syn. To monitor the kinetics of all three amyloid aggregation phases (*i.e.*, the lag, growth and plateau phases) in a single assay, in the absence of LLPS, it was necessary to incubate α-syn with ThT under aggregation promoting conditions, *i.e.*, shaking in the presence of a glass bead at 37 °C (**Fig. 4A** and **Supplementary Fig. 23**). We fitted the fluorescence data with a sigmoidal model to derive the time of the lag phase (t_{lag}) and the growth rate (HillSlope value) of aggregation. We found that 5-140 α-syn had a significantly shorter lag phase (~ 5.5-times faster t_{lag}), while those of 11-140 and 19-140 α-syn were comparable to FL α-syn (~ 1.5- and 1.1-times slower t_{lag}, respectively) (**Fig. 4A**,**B**). All truncated variants displayed significantly slower growth rates than FL α-syn (**Fig. 4A**,**C**). Given the short lag-phase of 5-140 α-syn, we monitored aggregation kinetics at varied FL and 5-140 α-syn concentrations, such that the scaling exponent (γ), and thus dominant aggregation mechanism could be predicted using the AmyloFit software[61]. We found that while FL α-syn displayed fragmentation-dominated aggregation kinetics, *i.e.*, a linear double logarithmic plot with γ ~ 0.5, 5-140 α-syn exhibited an increase in the contribution of secondary nucleation (**Supplementary Fig. 24)**[61].

Subsequently, we quantified the percentage of monomeric protein converted into aggregates during the assay. We found similar amounts of soluble protein remained at the end of aggregation for all variants (~10–20 % of the initial monomer), indicating a similar conversion of monomers into aggregates (**Supplementary Fig. 25**). Finally, we characterized the morphology and size of the aggregates by performing TEM on the insoluble protein fractions isolated after the aggregation assay (**Fig. 4D** and **Supplementary Fig. 26** and **27**). Although all variants formed rod-like amyloids, 11-140 and 19-140 α-syn fibrils did not display any twisting. Quantitative analysis of the TEM images highlighted that while FL and 5-140 α-syn fibrils were similar in length, 11-140 and 19-140 α-syn amyloids were typically shorter (**Fig. 4D** and **Supplementary Fig. 26** and **27**). Thus, increasing N-terminal truncation appears to reduce the structural stability of α-syn fibrils. This result is consistent with existing evidence that truncation of the first 6 N-terminal residues reduces fibril stability against mechanical agitation and protease activity[44]. As the amyloids

formed during our assay experience significant mechanical agitation due to shaking, our data indicate that residues 5 and 6 may facilitate the formation of amyloids with enhanced resistance to mechanical stress-induced fragmentation.

5-140 and FL α-syn fibrils also shared a comparable width distribution, while both 11-140 and 19-140 α-syn amyloids were significantly thinner (**Fig. 4D** and **Supplementary Fig. 26** and **27**). Hence, 11-140 and 19-140 α-syn fibrils were likely at an earlier maturation stage, *i.e.*, protofilaments and or protofibrils. This theory is supported by the high degree of fibrillar clumping observed for 11-140 and 19-140 α-syn, where many thin fibrils clustered together into large bundles (**Fig. 4D** and **Supplementary Fig. 26**). Such bundles may result from non-specific interactions between exposed hydrophobic regions on the protofilaments/protofibrils. Our findings are consistent with the inability of 7-140 α-syn to form thick fibrils, as we have previously reported[44], indicating deletion of residues 5 and 6 arrests aggregation at an earlier maturation stage.

Together, our data demonstrate that N-terminal truncation has a widespread effect on the amyloid aggregation of α-syn.

The N-terminal region of α-syn regulates the interaction of monomers with lipid vesicles and fibrils. To further our understanding of the role played by the N-terminus in the lag and growth phases of α-syn self-assembly, we examined the individual microscopic aggregation mechanisms, primary and secondary nucleation, and fibril elongation, for each of our variants.

First, we evaluated the propensity of each variant to undergo fibril elongation, *i.e.*, monomer binding to the ends of pre-formed fibrils, by monitoring their aggregation at neutral pH in the presence of long pre-formed fibrils[62,63]. All N-terminally truncated variants demonstrated strongly inhibited fibril elongation with respect to FL α-syn (**Fig. 4E**). Thus, our data indicate that the first 4 residues of α-syn monomers are critical for their interaction with fibril ends, explaining the delayed growth phase observed during the overall aggregation assay.

To assess the ability of each variant to undergo heterogeneous primary nucleation, *i.e.*, interaction with lipid membranes, we monitored their aggregation in the presence of 100 nm DMPS lipid vesicles[64]. To instead investigate the secondary nucleation ability of the truncated variants, *i.e.*, monomer binding to the surface of pre-formed fibrils, we monitored their aggregation at low pH in the presence of short pre-formed fibrils[62,65]. To ensure that all pre-formed fibrils were structurally mature and homogeneous, we used fibrils made of FL α-syn, as the aggregates of N-terminally truncated α-syn arrest at different maturation stages (**Fig. 4D**). The size homogeneity of all pre-formed fibril seeds and lipid vesicles was confirmed by DLS (**Supplementary Fig. 28**). Under both conditions, all α-syn variants aggregated (**Fig. 4E**), suggesting that N-terminally truncated monomers can interact with lipid vesicles and fibril ends to some extent. Interestingly, we found that both nucleation mechanisms were significantly enhanced for 5-140 α-syn, consistent with the increased contribution of secondary nucleation to the aggregation kinetics predicted using AmyloFit (**Fig. 4E and Supplementary Fig. 24**). Given this variant lacks Asp2, it may experience decreased electrostatic repulsion towards the negatively charged DMPS lipid vesicles or C-terminal fuzzy coat on the surface of α-syn fibrils. The accelerated primary and secondary nucleation rates of 5-140 α-syn may explain why its LLPS-induced aggregation is faster than FL α-syn, despite the consistent condensate lifetime of these two proteins in the bulk solution.

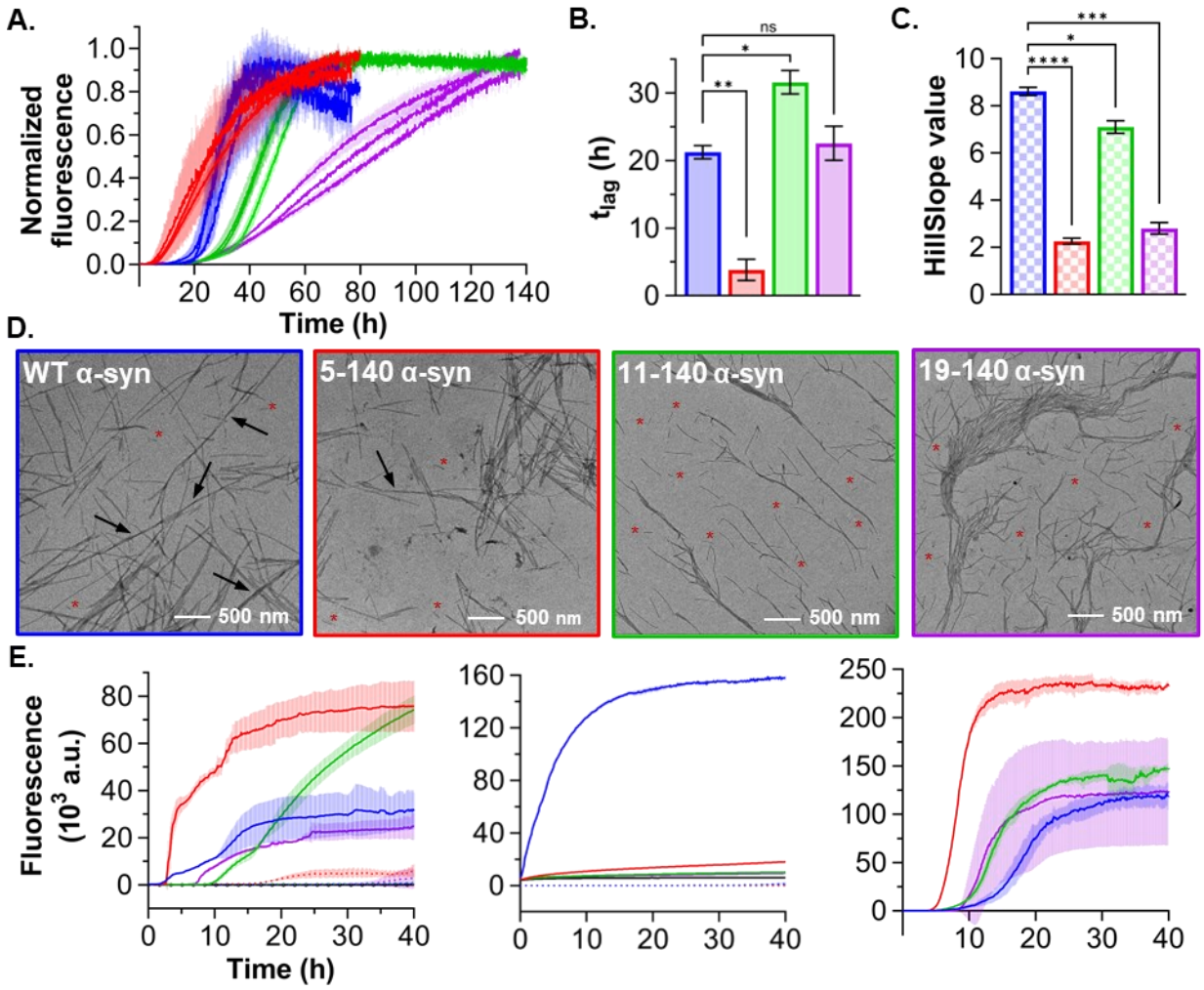

Figure 4. The microscopic steps of α-syn amyloid aggregation. A. The beaded aggregation of FL (blue), 5-140 (red), 11-140 (green) and 19-140 (purple) α-syn. Three individual biological replicates are shown. Each replicate is the mean of normalized technical replicates, n ≥ 2, where semi-transparent error bars represent the standard deviation. Samples were incubated at 37 °C under quiescent conditions in PBS (pH 7.4). **B/C.** The t_{lag} (**B.**) and HillSlope (**C.**) values of FL (blue), 5-140 (red), 11-140 (green) and 19-140 (purple) α-syn. Error bars represent the standard error of n = 3 biological replicates. **D.** Representative TEM images of the insoluble fraction after a beaded aggregation of either FL, 5-140, 11-140 or 19-140 α-syn. Short fibrils are highlighted by a red asterisk and fibril twists are indicated by an arrow. **E.** The aggregation of FL (blue), 5-140 (red), 11-140 (green) and 19-140 (purple) α-syn under conditions promoting interaction with lipid vesicles or pre-formed fibrils, either at their ends or surface. Left, the lipid-induced aggregation of α-syn in the presence (bold line) and absence (dashed line) of 100 nm DMPS lipid vesicles in PB (pH 6.5), alongside lipid vesicles alone as a control (black). Middle, the fibril elongation of α-syn in the presence (bold line) and absence (dashed line) of short pre-formed FL α-syn fibril seeds in PBS (pH 7.4), alongside fibril seeds alone as a control (black). Right, the secondary nucleation of α-syn in the presence of long pre-formed FL α-syn fibril seeds in 20 mM sodium acetate (pH 4.8), alongside the fibril seeds alone as a control (black). All assays were performed at 37 °C under quiescent conditions. Each dataset is a single representative biological repeat, the mean and standard deviation (represented by semi-transparent error bars) are shown, n = 3. Where appropriate, statistical significance was measured using a Welch and Brown-Forsythe ANOVA with multiple comparisons against the control (FL α-syn); $^{ns}p \geq 0.05$, $0.01 \leq {}^{*}p < 0.05$, $0.001 \leq {}^{**}p < 0.01$, $0.0001 \leq {}^{***}p < 0.001$ and $^{****}p < 0.0001$.

CONCLUSIONS

To investigate the consequences of N-terminal truncation on α-syn LLPS, here we develop a strategy combining the use of microscopy and a microplate reader to quantify condensate formation, maturation, and amyloid aggregation. We show that N-terminal truncation has a significant effect on condensate maturation (**Fig. 3**) and propose that N-terminal truncation inhibits condensate growth mechanisms and surface wetting, which in turn prolongs the existence of high surface:volume ratio condensates in solution, promoting condensate surface-catalyzed nucleation and, thus, aggregation of α-syn[58].

The notable exception to this trend was the pathological variant[18] 5-140 α-syn, which displayed a consistent condensate lifetime in solution to FL α-syn, yet underwent accelerated aggregation (**Fig. 3**). Investigation into the microscopic mechanisms of aggregation found that 5-140 α-syn has a significantly enhanced ability to undergo surface catalyzed nucleation (**Fig. 4**), which likely causes rapid nucleation at the condensate interface, accelerating aggregation following LLPS.

Here, we identify key regions of the early N-terminus in α-syn condensate maturation and surface-catalyzed nucleation. Our designed techniques and findings establish a robust foundation for future investigations into the microscopic mechanisms mediating α-syn LLPS and aggregation.

METHODS

Protein expression and purification. FL α-syn (residues 1-140) was expressed and purified as detailed previously[44]. Briefly, pT7-7 α-syn FL plasmid (a gift from Hilal Lashuel, Addgene[66]) was transformed into BL21-Gold (DE3) competent *Escherichia coli* (*E. coli*) cells (Agilent Technologies) according to the manufacturer's instructions and previous methodology[44]. Transformed cells were grown (37 °C, 200 rpm shaking) in LB media containing ampicillin (100 µg/ml) to an OD_{600} of ~ 0.7 before FL α-syn expression induced with 1 mM IPTG overnight (28 °C, 200 rpm shaking). The cells were then harvested by centrifugation and resuspended in buffer A (20 mM Tris-HCl, 1 mM EDTA, pH 8.0) including a protease inhibitor tablet (EDTA-free, Roche). Cells were lysed by sonication on ice before cell debris was removed by centrifuged (18,000 rpm, 45 min). The lysate was then boiled at 80 °C for 20 min, followed by another round of centrifugation (18,000 rpm, 30 min). Next, streptomycin sulphate (10 mg/ml) was gradually introduced to the supernatant. The mixture was incubated with rotation before further centrifugation (18,000 rpm, 30 min). FL α-syn was precipitated by the slow addition of ammonium sulphate (360 mg/ml) on ice, followed by incubation with rotation, and a final centrifugation (18,000 rpm, 30 min). The pellet was collected, re-suspended and dialyzed into buffer A overnight. The sample was then loaded onto an anion exchange chromatography column (HiPrep Q HP 16/10, Cytiva, USA) and further purified using a gradient elution with buffer B (20 mM Tris-HCl, 1 M NaCl, 1 mM EDTA, pH 8.0). The FL α-syn protein fractions, as determined by sodium dodecyl sulphate–polyacrylamide gel electrophoresis (SDS-PAGE), were then dialyzed into phosphate buffered saline (PBS, pH 7.4) overnight, before being passed through a gel filtration column (HiLoad 26/600 Superdex 75 pg, Cytiva, USA). The pure fractions, determined by SDS-PAGE, were combined and the concentration determined by Ultraviolet–visible (UV-Vis) spectroscopy absorbance at 275 nm (ε_{275nm} = 5600 $M^{-1}cm^{-1}$).

To generate 11-140 and 19-140 α-syn, deletion polymerase chain reaction (PCR) was performed on the pT7-7 Int7-140αSyn plasmid, which encodes a protein sequence where an intein is fused to the N-terminus of residues 7-140 of α-syn[44], eliminating the need for a non-native starting Met in the protein sequences. PCR was carried out using the Q5 high-fidelity DNA polymerase (New England Biolabs), the 5' phosphorylated primer pairs and their corresponding annealing temperatures (T_a), listed in Table 1. The template DNA was then digested with DpnI (New England Biolabs). Following sample purification using a NucleoSpin Gel and PCR Clean-up kit (MACHEREY-NAGEL), T4 DNA ligase (New England Biolabs, USA) was used to ligate the 5' phosphorylated blunt-end DNA fragments. All steps were carried out according to the relevant manufacturer's instructions. The resultant plasmids were then transformed into XL10-Gold Ultracompetent *E. coli* cells and purified using a QIAprep Spin Miniprep Kit. Mutagenesis success was determined by sequencing (GENEWIZ). Following several failed attempts to generate the 11-140 α-syn plasmid, Genscript performed the mutagenesis on our behalf.

Both variant plasmids were then transformed into BL21-Gold (DE3) cells, we found that increasing initial incubation on ice from 30 to 90 min increased transformation efficiency. The intein-α-syn fusion proteins corresponding to 11-140 and 19-140 α-syn were then expressed and the cell lysate harvested as described for FL α-syn. Subsequently, the fusion proteins were immobilized on a chitin resin before the target α-syn variant was cleaved, eluted and further purified by size-exclusion chromatography as previously described[44].

The N-terminal residue of 5-140 α-syn is Met and so the variant does not require intein conjugated expression. To generate the mutated plasmid the above deletion PCR process was applied to the pT7-7 α-syn WT plasmid using the 5' phosphorylated primer pair listed in Table 1. 5-140 α-syn was then expressed and purified as detailed for the FL protein.

Fluorescent labelling. FL α-syn was covalently tagged at its lysine residues using NHS-Rhodamine (ex. 552 nm, em. 575 nm, Thermo Scientific). The probe was added to 100 µM α-syn in ~ 8-fold molar excess, and the reaction was allowed to proceed at RT (~ 4 h, gentle mixing). Subsequently, excess dye was removed by extensive dialysis into PBS, pH 7.4 (overnight, 4 °C). For the purpose of subsequent assays, it was sufficient to assume no significant change in α-syn concentration had occurred during this process.

Electrospray ionization mass spectrometry. Purified protein samples (~ 50 μM, diH_2O) were analyzed by electrospray ionization mass spectrometry (ESI-MS). ESI-MS was performed by Lisa Haigh, Malgorzata Puchnarewicz and Adriana Lobosco using the Chemistry Mass Spectrometry facilities available at the Molecular Sciences Research Hub, Department of Chemistry, Imperial College London. The spectra were plotted using GraphPad Prism version 10.0.3 (GraphPad Software).

Differential interference contrast and fluorescence microscopy. To assess the LLPS behavior of α-syn, the protein was incubated with PEG-8000 and PLK, conditions previously shown to induce α-syn LLPS[53]. PEG-8000 was dissolved in PBS, pH 7.4 to a concentration of 20 % w/v. PLK hydrochloride (Merck, Germany) with a molecular weight of 15,000–30,000 g/mol was dissolved in 10 mM HEPES, 100 mM NaCl, pH 7.4 to a concentration of 3 mM (determined using an approximate molecular weight of 22,500 g/mol). LLPS was induced by incubating monomeric protein (0, 20, 40 and 60 μM) with PLK (0, 25, 50 and 100 μM) in LLPS buffer (PBS, pH 7.4, 10 % PEG-8000, 0.02 % NaN_3). 5 minutes after PLK addition, 100 μl of sample (single replicate per assay) was loaded into a 96 well full-area glass bottom plate (Sensoplate, Greiner Bio One, Austria). The plate was covered with a clear, microscopy compatible self-adhesive film (ibiSeal, Ibidi, Germany). The film was secured onto the plate using strips of adhesive aluminum foil along each edge. The samples were incubated at 37 °C within the chamber of a Nikon ECLIPSE Ti2-E microscope (Nikon, Japan) and automated DIC microscopy imaging was carried out 15 min from PLK addition using a 40x air objective. A z-stack (3-step, 200 μm step size) within the bulk solution was acquired per well.

Condensate maturation in samples containing monomeric α-syn (0 or 60 μM) and PLK (0 or 25 μM) was monitored at 37 °C using the above automated imaging at pre-determined time points over a 20 h incubation period. Endpoint (bottom of well or in solution) DIC images were manually captured after the 20 h time point. When stated, 20 μM ThT was included to monitor amyloid fibril formation, and fluorescence images were taken alongside DIC images using excitation 405 nm and emission 515/30 nm filters. Unless otherwise stated a 40x air objective was used.

Both the 15 min and time course DIC images underwent processing, which involved estimating the number of objects per image and the area of every object in a given image. This analysis was conducted using GA3 software integrated into the NIS-Elements software (Nikon, Japan). A detailed GA3 recipe is provided in **Supplementary Fig. 4**. In brief, images were first subjected to denoising to reduce shot noise. Objects were identified within the images by defining a gain thresholding range. To enhance accuracy, border objects and objects exceeding 50 μm² in area (larger than the maximum condensate area determined through manual inspection) were excluded. The compiled object area values and the total number of objects per image, across all z positions, per well, and time point were consolidated into a single data table.

Phase diagrams were generated using the normalized total number of objects counted per well, summed over all z positions, 15 min from PLK addition. To examine the time course experiments, the area distribution of each sample, compiled over all z positions, at each time point was plotted. The mean area at each time point was determined, plotted against time, and normalized. Three separate biological repeats were globally fitted with a one-phase association curve. The half-time (t_{50}) of object growth was derived. Next, the total object count at each time point, compiled over all z positions, was plotted against time and normalized. Three separate biological repeats were globally fitted with a one-phase decay curve and the half-time (t_{50}) of count decay was derived. Normalization of the object count and mean object area values was performed to account for inherent variations in their absolute values arising from manual error when defining the thresholding range. All data were plotted using GraphPad Prism version 10.0.3.

FL α-syn localization was monitored using a 1:100 ratio of rhodamine labeled: unlabeled FL α-syn. Fluorescence images were taken alongside DIC images using excitation 525 nm and emission 641/75 nm filters. A single sample was prepared at a time, loaded into a 96 well full-area glass bottom plate, and imaged manually using a 40x air objective.

Aggregation assay under liquid-liquid phase separation conditions. Fibril formation was monitored by incubation of monomeric α-syn (0 and 60 μM) with PLK (0 and 25 μM) and 20 μM ThT in LLPS buffer. 100 μl of sample (3 replicates) was loaded into a 96 well full-area glass bottom plate, sealed with aluminum foil, and incubated at 37 °C under quiescent conditions for ~ 70 h in a CLARIOstar Plus microplate reader. Fluorescent intensity measurements were taken at the center of the well, excitation 440-10 nm, dichroic 460 nm and emission 480-10 nm filters, 2 gains and 30 flashes per well, every 20 min. The data were plotted using GraphPad Prism version 10.0.3.

Transmission election microscopy. A sample of the washed insoluble fraction taken at the endpoint of a beaded aggregation assay, or of the whole solution taken at the endpoint of an aggregation assay under LLPS conditions, was applied to carbon films on 300 mesh copper grids (Agar Scientific Ltd., UK). The grids were quickly washed with diH_2O, negatively stained with 2 % (w/v) uranyl acetate and washed again. The grids were imaged using the Tecnai 12 Spirit transmission electron microscope (Thermo Fisher Scientific (formerly FEI), USA) available at the Electron Microscopy

Centre, Centre of Structural Biology, Imperial College London. Where specified fibril lengths and widths were measured using Fiji, with the data plotted using GraphPad Prism version 10.0.3.

Dot-blot analysis. The presence of α-syn in the insoluble aggregates formed following aggregation under LLPS conditions was determined by dot-blot analysis. The soluble and insoluble protein fractions at the endpoint of the aggregation assay were separated by centrifugation (30 min, 14,000 rpm). The insoluble pellet was resuspended in a minimum volume of PBS before 5 replicates of 3 µl aliquots were transferred to a nitrocellulose membrane (0.45 µm) and allowed to dry. The membrane was then blocked (1 h, 4 °C) with a solution of milk powder (5 %) dissolved in PBS-T (PBS supplemented with 0.1 % Tween 20). After washing with PBS-T, the membrane was incubated (overnight, 4 °C) with the anti-α-syn primary antibody MJFR1 (diluted 1:1000 in PBS-Tween, Abcam, UK). Following rigorous washing with PBS-T, the membrane was incubated (1 h, RT) with the goat anti-rabbit IgG (H + L) highly cross adsorbed secondary antibody, conjugated to the fluorophore Alexa Fluor plus 555 (diluted 1:5000 in PBS-Tween, Thermo Fisher Scientific, USA). Finally, the membrane was washed with PBS-T and imaged with a Typhoon FLA 9000 (Cytiva, USA). As a control, the same dot-blot protocol was used to analyze the reactivity of the primary antibody against 25 µM PLK in PBS.

Circular dichroism. The far-UV circular dichroism (CD) spectra of fresh monomeric protein (20 µM) or the insoluble aggregate pellet (~ 10 µM) taken from the endpoint of a ThT aggregation assay under LLPS conditions were recorded. The insoluble fractions were obtained by centrifugation, and their concentration estimated using UV-Vis spectroscopy absorbance at 275 nm (ε_{275nm} = 5600 $M^{-1}cm^{-1}$) following denaturation in 4 M guanidinium chloride for 2 h at RT. Spectra of all samples were taken using a Chirascan v100 (Applied Photophysics Ltd, UK) from 200 to 250 nm with a 0.5 nm step, 1 nm bandwidth, 1 s per time point and 5 accumulations. A PBS background spectrum was subtracted from each sample spectrum. For monomeric protein samples the raw data (in mdeg) were converted to mean residue ellipticity (MRE, units deg cm^2 $dmol^{-1}$) using[67]:

$$\mathbf{MRE} = \mathbf{mdeg} \div \left(\mathbf{l} \times \mathbf{c} \times (\mathbf{n} - \mathbf{1})\right) \qquad \text{equation (1)}$$

where mdeg is the raw data (in mdeg), l is the cuvette pathlength (in mm), c is the sample concentration (in M) and n is the number of amino acids. The data were plotted using GraphPad Prism version 10.0.3.

Monomer conversion analysis. The soluble and insoluble protein fractions before and after a beaded aggregation assay were separated by centrifugation (30 min, 16,900 x g). The soluble fraction was then extracted and analyzed by SDS-PAGE. For each sample, the mean grey value of the band corresponding to the relevant monomeric protein variant was measured using Fiji[68]. Percentage conversion of monomer into insoluble aggregates was estimated by comparison of the band intensity before and after aggregation. The data were plotted using GraphPad Prism version 10.0.3.

Beaded aggregation assay. To monitor all three phases in the amyloid aggregation, monomeric protein was aggregated and monitored by fluorescence spectroscopy using a previously described protocol[44]. Briefly, monomer solutions (50 µM) were aggregated with ThT (20 µM) and NaN_3 (0.02 %) in PBS (pH 7.4). 170 µl of sample (in triplicate) was loaded into a 96 well full-area µClear plate (non-binding, clear bottomed, #655906, Greiner Bio-One, Austria), sealed with an aluminium film and incubated at 37 °C for ~ 70 - 140 h in a CLARIOstar Plus microplate reader (BMG Labtech, Germany). Aggregation was promoted by linear shaking (300 rpm, 300 s before each cycle) and addition of a single borosilicate bead (3 mm diameter) per well. Fluorescent intensity measurements were taken every 520 s using spiral averaging (5 mm diameter) and excitation 440 nm, dichroic 460 nm, and emission 480 nm filters, 3 gains and 50 flashes per well.

The data were plotted using GraphPad Prism version 10.0.3. The individual biological replicates were fit with sigmoidal, 4PL, X is concentration standard curves provided by the software. t_{50} was estimated as the time (x-value) at which 50 % maximum fluorescence intensity was reached. t_{lag} was estimated by extrapolation of the tangent at t_{50}. The steepness of the curve was estimated by the Hillslope value, where Prism assigns a standard sigmoidal receptor binding curve a Hillslope value of 1.0, while a steeper curve has a higher Hillslope value, and a shallower curve has a lower Hillslope value.

To estimate γ for FL and 5-140 α-syn, this assay was repeated with 10, 25, 50, 75 and 100 µM protein. The data were uploaded to AmyloFit 2.0 where the log of initial monomer concentration (m_0) was calculated alongside the log of the half-life of aggregation (t_{50})[61]. All data were plotted using GraphPad Prism. The double logarithmic plot was fitted with a simple linear regression and g estimated as the gradient. As γ is not constant for 5-140 α-syn, the data was fit with two straight lines corresponding to two different γ values.

Lipid-induced aggregation assay. Lipid vesicles were produced based on a previously described protocol[64]. Briefly, 1,2-dimyristoyl-sn-glycero-3-phospho-L-serine (sodium salt) (DMPS, Merck) was dissolved in 20 mM phosphate buffer

(PB), pH 6.5 at ~ 70 °C for 2 h. The lipids were then freeze-thawed using liquid nitrogen and a ~ 50 °C water bath 5 times before being extruded 11 times through a membrane (100 nm pore diameter) at ~ 70 °C. Subsequently, monomer solutions (50 μM) were aggregated in PB (pH 6.5) in the presence and absence of DMPS lipid vesicles (250 μM), ThT (20 μM) and NaN3 (0.02 %). 170 μl of each sample (3 replicates) was loaded into a 96 well full-area μClear plate, sealed with aluminum foil, and incubated at 37 °C for ~ 40 h in a FLUOstar Omega microplate reader (BMG Labtech, Germany). Fluorescent intensity measurements were taken using spiral averaging (3 mm diameter), excitation 440-10 nm, dichroic 460 nm and emission 480-10 nm filters, 4 gains and 50 flashes per well. The size homogeneity of the lipid vesicles was determined by dynamic light scattering (DLS, Zetasizer Ultra, Malvern Panalytical, UK). All data were plotted using GraphPad Prism version 10.0.3.

Seeded aggregation assay. Pre-formed fibril seeds were generated by shaking (~ 600 rpm) monomeric FL α-syn (~ 200 μM, PBS, pH 7.4) at 37 °C for ~ 5–10 days. NaN_3 (0.02 %) was added to prevent bacterial growth during prolonged incubation. The soluble and insoluble protein fractions were then separated by centrifugation (30 min, 14,000 rpm), the soluble fraction removed, and the pellet resuspended in fresh PBS, pH 7.4. Centrifugation and pellet resuspension were repeated before the final protein concentration was estimated using UV-Vis spectroscopy absorbance at 275 nm (ε_{275nm} = 5600 $M^{-1}cm^{-1}$) after denaturation in 4 M guanidinium chloride for 2 h at RT.

Seeded aggregation assays were carried out based on previously described protocols[63,69]. Immediately before use the pre-formed FL α-syn fibril stock was diluted to ~ 100 μm in PBS (pH 7.4) and the precise concentration measured by UV-Vis spectroscopy. When performing a fibril elongation assay, this pre-formed fibril solution was then diluted to 50 μM in PBS, pH 7.4 and probe sonicated on ice at 20 % power, 15 s pulse, 15 s rest for 4 cycles. Monomeric protein (50 μM) was then incubated with these short pre-formed FL α-syn fibrils (5 μM), ThT (20 μM) and NaN_3 (0.02 %) in PBS, pH 7.4.

To perform secondary nucleation experiments, the ~ 100 μm pre-formed fibril stock was diluted to 5 μM in 20 mM acetic acid (NaCl 150 mM, pH 4.8) and probe sonicated on ice at 20% power, 5 s pulse, 5 s rest, 3 cycles. Monomeric protein (50 μM) was also buffer exchanged into 20 mM acetic acid (NaCl 150 mM, pH 4.8), and then incubated with these long pre-formed FL α-syn fibrils (50 nM), ThT (20 μM) and NaN3 (0.02 %).

For both assays, 170 μl of sample (3 replicates) was loaded into a 96 well full-area μClear plate, sealed with aluminum foil and incubated for ~ 40 h at 37 °C in a FLUOstar Omega microplate reader under quiescent conditions. Fluorescent intensity measurements were taken using the settings described above for the lipid-induced aggregation assay. The size homogeneity of any sonicated pre-formed fibril seeds was determined by DLS. All data were plotted using GraphPad Prism version 10.0.3.

ASSOCIATED CONTENT

Supporting Information

Supplementary figures can be found in the Supplementary Information file.

AUTHOR INFORMATION

Corresponding Author

*Email: f.aprile@imperial.ac.uk, Phone: +44 (0)20 7594 5545

ORCID iD

Rebecca J. Thrush: 0000-0001-7783-954X
Devkee M. Vadukul: 0000-0003-2073-0089
Siân C. Allerton: 0009-0005-6156-6707
Marko Storch: 0000-0003-1503-8282
Francesco A. Aprile: 0000-0002-5040-4420

Author Contributions

RJT, DMV and SCA performed all experiments. RJT and FAA analyzed the data. RJT and FAA conceptualized the work. All authors discussed the data and provided feedback on the manuscript.

Funding Sources

We thank UK Research and Innovation (Future Leaders Fellowship MR/S033947/1 and MR/Y003616/1), the Alzheimer's Society, UK (Grant 511), and Alzheimer's Research UK (ARUK-PG2019B-020) for support. R.J.T. was supported by a scholarship by the Department of Chemistry (Imperial College London).

ACKNOWLEDGMENTS
We thank Prof. Dr. Paolo Arosio (ETH Zurich) for helpful discussions and feedback on the manuscript. We also thank the Chemistry Mass Spectrometry facilities for assistance with ESI-MS, and the Electron Microscopy Centre facilities at The Center of Structural Biology for assistance with TEM.

ABBREVIATIONS
IDP, intrinsically disordered protein; α-syn, α-synuclein; PD, Parkinson's disease; NAC, non-amyloid-β component; PTMs, post-translational modifications; LLPS, liquid-liquid phase separation; PEG, poly-ethylene glycol; PLK, poly-L-lysine; FL, full length; hnRNPA1, heterogeneous nuclear ribonucleoprotein A1; *E. coli*, *Escherichia coli*; SDS-PAGE, sodium dodecyl sulphate–polyacrylamide gel electrophoresis; PBS, phosphate buffered saline; UV-Vis, Ultraviolet–visible; PCR, polymerase chain reaction; ESI-MS, electrospray ionization mass spectrometry; DMPS, 1,2-dimyristoyl-sn-glycero-3-phospho-L-serine (sodium salt); PB, 20 mM phosphate buffer; ThT, Thioflavin T; DLS, dynamic light scattering; DIC, differential interference contrast; GA3, General Analysis 3; TEM, transmission electron microscopy.

REFERENCES
1 Weinreb, P. H., Zhen, W., Poon, A. W., Conway, K. A. & Lansbury, P. T. NACP, a protein implicated in Alzheimer's disease and learning, is natively unfolded. *Biochemistry* **35**, 13709-13715 (1996).
2 Maroteaux, L., Campanelli, J. T. & Scheller, R. H. Synuclein: a neuron-specific protein localized to the nucleus and presynaptic nerve terminal. *J. Neurosci.* **8**, 2804-2815 (1988).
3 Duce, J. A. *et al.* Post translational changes to α-synuclein control iron and dopamine trafficking; a concept for neuron vulnerability in Parkinson's disease. *Mol. Neurodegener.* **12**, 1-12 (2017).
4 Cheng, F., Vivacqua, G. & Yu, S. The role of alpha-synuclein in neurotransmission and synaptic plasticity. *J. Chem. Neuroanat.* **42**, 242-248 (2011).
5 Burré, J., Sharma, M. & Südhof, T. C. α-Synuclein assembles into higher-order multimers upon membrane binding to promote SNARE complex formation. *Proc. Natl. Acad. Sci.* **111**, E4274-E4283 (2014).
6 Uversky, V. N., Li, J. & Fink, A. L. Evidence for a partially folded intermediate in α-synuclein fibril formation. *J. Biol. Chem.* **276**, 10737-10744 (2001).
7 Bartels, T., Choi, J. G. & Selkoe, D. J. α-Synuclein occurs physiologically as a helically folded tetramer that resists aggregation. *Nature* **477**, 107-110 (2011).
8 Mor, D. E., Ugras, S. E., Daniels, M. J. & Ischiropoulos, H. Dynamic structural flexibility of α-synuclein. *Neurobiol. Dis.* **88**, 66-74 (2016).
9 Tuttle, M. D. *et al.* Solid-state NMR structure of a pathogenic fibril of full-length human α-synuclein. *Nat. Struct. Mol. Biol.* **23**, 409-415 (2016).
10 Miake, H., Mizusawa, H., Iwatsubo, T. & Hasegawa, M. Biochemical characterization of the core structure of α-synuclein filaments. *J. Biol. Chem.* **277**, 19213-19219 (2002).
11 Der-Sarkissian, A., Jao, C. C., Chen, J. & Langen, R. Structural organization of α-synuclein fibrils studied by site-directed spin labeling. *J. Biol. Chem.* **278**, 37530-37535 (2003).
12 Li, Y. *et al.* Amyloid fibril structure of α-synuclein determined by cryo-electron microscopy. *Cell Res.* **28**, 897-903 (2018).
13 Spillantini, M. G. *et al.* α-Synuclein in Lewy bodies. *Nature* **388**, 839-840 (1997).
14 Spillantini, M. G. *et al.* Filamentous α-synuclein inclusions link multiple system atrophy with Parkinson's disease and dementia with Lewy bodies. *Neurosci. Lett.* **251**, 205-208 (1998).
15 Pancoe, S. X. *et al.* Effects of mutations and post-translational modifications on α-synuclein in vitro aggregation. *J. Mol. Biol.*, 167859 (2022).
16 Oueslati, A. Implication of alpha-synuclein phosphorylation at S129 in synucleinopathies: what have we learned in the last decade? *J. Parkinsons Dis.* **6**, 39-51 (2016).
17 Anderson, J. P. *et al.* Phosphorylation of Ser-129 is the dominant pathological modification of α-synuclein in familial and sporadic Lewy body disease. *J. Biol. Chem.* **281**, 29739-29752 (2006).
18 Kellie, J. F. *et al.* Quantitative measurement of intact alpha-synuclein proteoforms from post-mortem control and Parkinson's disease brain tissue by intact protein mass spectrometry. *Sci. Rep.* **4**, 1-10 (2014).
19 Killinger, B. A. *et al.* The vermiform appendix impacts the risk of developing Parkinson's disease. *Sci. Transl. Med.* **10** (2018).
20 Chakroun, T. *et al.* Alpha-synuclein fragments trigger distinct aggregation pathways. *Cell Death Dis.* **11**, 1-16 (2020).
21 Hoyer, W., Cherny, D., Subramaniam, V. & Jovin, T. M. Impact of the acidic C-terminal region comprising amino acids 109− 140 on α-synuclein aggregation in vitro. *Biochemistry* **43**, 16233-16242 (2004).
22 Izawa, Y. *et al.* Role of C-terminal negative charges and tyrosine residues in fibril formation of α-synuclein. *Brain and behavior* **2**, 595-605 (2012).

23 van der Wateren, I. M., Knowles, T. P., Buell, A. K., Dobson, C. M. & Galvagnion, C. C-terminal truncation of α-synuclein promotes amyloid fibril amplification at physiological pH. *Chemical science* **9**, 5506-5516 (2018).
24 Sorrentino, Z. A. *et al.* Physiological C-terminal truncation of α-synuclein potentiates the prion-like formation of pathological inclusions. *J. Biol. Chem.* **293**, 18914-18932 (2018).
25 Levitan, K. *et al.* Conserved C-terminal charge exerts a profound influence on the aggregation rate of α-synuclein. *J. Mol. Biol.* **411**, 329-333 (2011).
26 Serpell, L. C., Berriman, J., Jakes, R., Goedert, M. & Crowther, R. A. Fiber diffraction of synthetic α-synuclein filaments shows amyloid-like cross-β conformation. *Proc. Natl. Acad. Sci.* **97**, 4897-4902 (2000).
27 Bell, R. *et al.* N-Terminal Acetylation of α-Synuclein Slows down Its Aggregation Process and Alters the Morphology of the Resulting Aggregates. *Biochemistry* **61**, 1743-1756 (2022).
28 Kang, L. *et al.* N-terminal acetylation of α-synuclein induces increased transient helical propensity and decreased aggregation rates in the intrinsically disordered monomer. *Protein Sci.* **21**, 911-917 (2012).
29 Watson, M. D. & Lee, J. C. N-terminal acetylation affects α-synuclein fibril polymorphism. *Biochemistry* **58**, 3630-3633 (2019).
30 Vlad, C. *et al.* Autoproteolytic fragments are intermediates in the oligomerization-aggregation of Parkinson's disease protein alpha-synuclein as revealed by ion mobility mass spectrometry. *Chembiochem* **12**, 2740 (2011).
31 Vlad, C., Iurascu, M. I., Slamnoiu, S., Hengerer, B. & Przybylski, M. in *Intrinsically Disordered Protein Analysis* (ed Vladimir N Uversky, A.K. Dunker) 399-412 ((Springer, 2012).
32 Liu, C.-W. *et al.* A precipitating role for truncated α-synuclein and the proteasome in α-synuclein aggregation: implications for pathogenesis of Parkinson disease. *J. Biol. Chem.* **280**, 22670-22678 (2005).
33 Dufty, B. M. *et al.* Calpain-cleavage of α-synuclein: connecting proteolytic processing to disease-linked aggregation. *Am. J. Pathol* **170**, 1725-1738 (2007).
34 Li, W. *et al.* Aggregation promoting C-terminal truncation of α-synuclein is a normal cellular process and is enhanced by the familial Parkinson's disease-linked mutations. *Proc. Natl. Acad. Sci.* **102**, 2162-2167 (2005).
35 Grassi, D. *et al.* Identification of a highly neurotoxic α-synuclein species inducing mitochondrial damage and mitophagy in Parkinson's disease. *Proc. Natl. Acad. Sci.* **115**, E2634-E2643 (2018).
36 Lee, H.-J., Choi, C. & Lee, S.-J. Membrane-bound α-synuclein has a high aggregation propensity and the ability to seed the aggregation of the cytosolic form. *J. Biol. Chem.* **277**, 671-678 (2002).
37 McLean, P. J., Kawamata, H., Ribich, S. & Hyman, B. T. Membrane association and protein conformation of α-synuclein in intact neurons: effect of Parkinson′ s disease-linked mutations. *J. Biol. Chem.* **275**, 8812-8816 (2000).
38 Fusco, G. *et al.* Direct observation of the three regions in α-synuclein that determine its membrane-bound behaviour. *Nat. Commun.* **5**, 1-8 (2014).
39 Leftin, A., Job, C., Beyer, K. & Brown, M. F. Solid-state 13C NMR reveals annealing of raft-like membranes containing cholesterol by the intrinsically disordered protein α-synuclein. *J. Mol. Biol.* **425**, 2973-2987 (2013).
40 Galvagnion, C. *et al.* Lipid vesicles trigger α-synuclein aggregation by stimulating primary nucleation. *Nat. Chem. Biol.* **11**, 229-234 (2015).
41 Kumari, P. *et al.* Structural insights into α-synuclein monomer–fibril interactions. *Proc. Natl. Acad. Sci.* **118** (2021).
42 Yang, X., Wang, B., Hoop, C. L., Williams, J. K. & Baum, J. NMR unveils an N-terminal interaction interface on acetylated-α-synuclein monomers for recruitment to fibrils. *Proc. Natl. Acad. Sci.* **118** (2021).
43 McGlinchey, R. P., Ni, X., Shadish, J. A., Jiang, J. & Lee, J. C. The N terminus of α-synuclein dictates fibril formation. *Proc. Natl. Acad. Sci.* **118** (2021).
44 Thrush, R. J., Vadukul, D. M. & Aprile, F. A. A Facile Method to Produce N-Terminally Truncated α-Synuclein. *Front. Neurosci.* **16**, 881480 (2022).
45 Lorenzen, N., Lemminger, L., Pedersen, J. N., Nielsen, S. B. & Otzen, D. E. The N-terminus of α-synuclein is essential for both monomeric and oligomeric interactions with membranes. *FEBS Lett.* **588**, 497-502 (2014).
46 Vamvaca, K., Volles, M. J. & Lansbury Jr, P. T. The first N-terminal amino acids of α-synuclein are essential for α-helical structure formation in vitro and membrane binding in yeast. *J. Mol. Biol.* **389**, 413-424 (2009).
47 Ray, S. *et al.* α-Synuclein aggregation nucleates through liquid–liquid phase separation. *Nat. Chem.* **12**, 705-716 (2020).
48 Sawner, A. S. *et al.* Modulating α-Synuclein Liquid-Liquid Phase Separation. *Biochemistry* (2021).
49 Lipiński, W. P. *et al.* Biomolecular condensates can both accelerate and suppress aggregation of α-synuclein. *Science advances* **8**, eabq6495 (2022).
50 Xu, B., Chen, J. & Liu, Y. Curcumin interacts with α-synuclein condensates to inhibit amyloid aggregation under phase separation. *ACS omega* **7**, 30281-30290 (2022).

51 Xu, B. *et al.* Manganese promotes α-synuclein amyloid aggregation through the induction of protein phase transition. *J. Biol. Chem.* **298** (2022).
52 Huang, S. *et al.* α-Synuclein phase separation and amyloid aggregation are modulated by C-terminal truncations. *FEBS Lett.* **596**, 1388-1400 (2022).
53 Gracia, P. *et al.* Molecular mechanism for the synchronized electrostatic coacervation and co-aggregation of alpha-synuclein and tau. *Nat. Commun.* **13**, 4586 (2022).
54 Dada, S. T. *et al.* Spontaneous nucleation and fast aggregate-dependent proliferation of α-synuclein aggregates within liquid condensates at neutral pH. *Proc. Natl. Acad. Sci.* **120**, e2208792120 (2023).
55 Molliex, A. *et al.* Phase separation by low complexity domains promotes stress granule assembly and drives pathological fibrillization. *Cell* **163**, 123-133 (2015).
56 Wen, J. *et al.* Conformational expansion of tau in condensates promotes irreversible aggregation. *J. Am. Chem. Soc.* **143**, 13056-13064 (2021).
57 Babinchak, W. M. *et al.* The role of liquid–liquid phase separation in aggregation of the TDP-43 low-complexity domain. *J. Biol. Chem.* **294**, 6306-6317 (2019).
58 Linsenmeier, M. *et al.* The interface of condensates of the hnRNPA1 low-complexity domain promotes formation of amyloid fibrils. *Nat. Chem.*, 1-10 (2023).
59 Küffner, A. M. *et al.* Sequestration within biomolecular condensates inhibits Aβ-42 amyloid formation. *Chemical Science* **12**, 4373-4382 (2021).
60 Emmanouilidis, L. *et al.* A solid beta-sheet structure is formed at the surface of FUS droplets during aging. *Nat. Chem. Biol.*, 1-9 (2024).
61 Meisl, G. *et al.* Molecular mechanisms of protein aggregation from global fitting of kinetic models. *Nat. Protoc.* **11**, 252-272 (2016).
62 Buell, A. K. *et al.* Solution conditions determine the relative importance of nucleation and growth processes in α-synuclein aggregation. *Proc. Natl. Acad. Sci.* **111**, 7671-7676 (2014).
63 Doherty, C. P. *et al.* A short motif in the N-terminal region of α-synuclein is critical for both aggregation and function. *Nat. Struct. Mol. Biol.* **27**, 249-259 (2020).
64 Galvagnion, C. *et al.* Chemical properties of lipids strongly affect the kinetics of the membrane-induced aggregation of α-synuclein. *Proc. Natl. Acad. Sci.* **113**, 7065-7070 (2016).
65 Gaspar, R. *et al.* Secondary nucleation of monomers on fibril surface dominates α-synuclein aggregation and provides autocatalytic amyloid amplification. *Q. Rev. Biophys.* **50**, e6 (2017).
66 Paleologou, K. E. *et al.* Phosphorylation at Ser-129 but not the phosphomimics S129E/D inhibits the fibrillation of α-synuclein. *J. Biol. Chem.* **283**, 16895-16905 (2008).
67 Greenfield, N. J. Using circular dichroism spectra to estimate protein secondary structure. *Nat. Protoc.* **1**, 2876-2890 (2006).
68 Schindelin, J. *et al.* Fiji: an open-source platform for biological-image analysis. *Nat. Methods* **9**, 676-682 (2012).
69 Flagmeier, P. *et al.* Mutations associated with familial Parkinson's disease alter the initiation and amplification steps of α-synuclein aggregation. *Proc. Natl. Acad. Sci.* **113**, 10328-10333 (2016).